Soft Matter

Accepted Manuscript
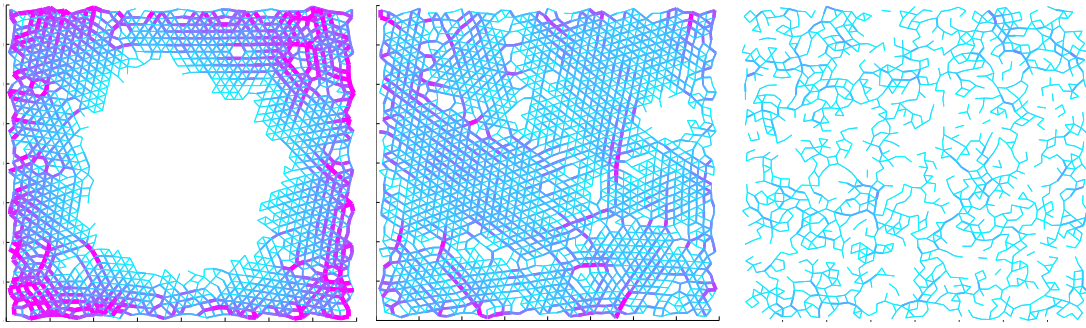
Our work represents a first step towards understanding the equation of state of active systems at high density.

Aggregation and Segregation of Confined Active Particles[†]

Xingbo Yang,[*a] **M. Lisa Manning,**[ab] **and M. Cristina Marchetti**[ab]

We simulate a model of self-propelled disks with soft repulsive interactions confined to a box in two dimensions. For small rotational diffusion rates, monodisperse disks spontaneously accumulate at the walls. At low densities, interaction forces between particles are strongly inhomogeneous, and a simple model predicts how these inhomogeneities alter the equation of state. At higher densities, collective effects become important. We observe signatures of a jamming transition at a packing fraction $\phi \sim 0.88$, which is also the jamming point for non-active athermal monodisperse disks. At this ϕ, the system develops a critical finite active speed necessary for wall aggregation. At packing fractions above $\phi \sim 0.6$, the pressure decreases with increasing density, suggesting that strong interactions between particles are affecting the equation of state well below the jamming transition. A mixture of bidisperse disks segregates in the absence of any adhesion, identifying a new mechanism that could contribute to cell sorting in embryonic development.

1 Introduction

Minimal models of self-propelled particles (SPP) have provided much insight into the emergent behavior of non-equilibrium, active systems where energy is injected at the scale of the individual constituents. This novel class of materials spans many length scales, ranging from bird flocks to bacterial swarms, cell layers and synthetic microswimmers[1]. Novel behaviors have been predicted theoretically and observed in simulations and experiments, including flocking[2], large density fluctuations[3,4], and spontaneous phase separation[5–7]. Walls and confined geometries are ubiquitous in realizations of active systems. For example, sperm and bacteria often live near surfaces or in narrow channels, and these interfaces strongly affect their dynamics[8–11]. Vibrated granular rods spontaneously accumulate at the walls even in the absence of hydrodynamic interactions[12,13]. Finally, mixtures of two types of active particles have been studied as minimal models of cell sorting in co-cultures and have been shown to segregate in bulk in the presence of adhesive interactions[14–16].

In this paper we study a minimal model of athermal self-propelled disks with soft repulsive interactions confined to a box in two dimensions. The soft repulsive potential is chosen to provide finite energy barriers to particle crossing, as a way to mimic living cells that are capable of escaping to the third dimension and cross over each other. Each disk performs a persistent random walk consisting of ballistic runs at speed v_0, randomized by rotational diffusion at rate D_r. We find that confined self-propelled particles aggregate at the walls provided their rotational diffusion is sufficiently slow (Fig. 1(a)). At low density, aggregation occurs when a particle travels ballistically across the container. At high packing fraction ϕ,
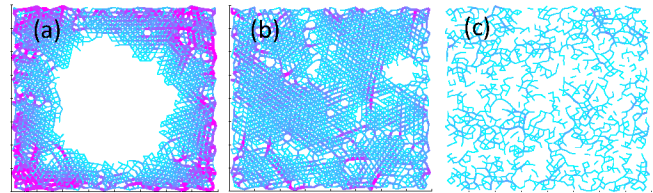

Fig. 1 Force chains at time $T = 2000$ for $v_0 = 0.02$ displaying (a) aggregation at $D_r = 5 \times 10^{-5}$ and $\phi = 0.672$, (b) jammed state at $D_r = 5 \times 10^{-5}$ and $\phi = 0.896$, and (c) homogeneous gas state at $D_r = 0.005$ and $\phi = 0.672$. (†Supplementary Movies 1-3)

however, a critical active speed $v_c(\phi)$ is required for wall aggregation even in the limit $D_r \to 0$. The onset of a nonzero value of v_c in our active material correlates with the packing fraction at which non-active hard disks become "jammed"[17], i.e. exhibit a non-zero yield stress. The pressure of the active fluid, like the density, is spatially inhomogeneous as the particles seem to organize to optimally transmit stresses to the walls, as shown in Fig. 1(a). As the jamming point is approached, the system becomes more uniform (Fig. 1(b)) and the pressure begins to decrease with increasing density. This decrease occurs well below the jamming point and is associated with the onset of slow relaxation times due to strong caging effects that occur over a broad range of densities due to their activity. This non-monotonic dependence of pressure on density is unique to active systems. It is consistent with the non-monotonic dependence of pressure on temperature in a thermal active gas[18] and on system size in a dilute active gas[19]. Finally, this aggregation can be harnessed in a mixture of self-propelled particles of different sizes that segregates in the absence of any alignment or attraction (Fig. 5). The sense of the segregation (i.e., whether the large or the small disks accumulate on the outside) is determined by a mean field calculation for the energy barrier generated by the repulsive interaction. This segregation is reminiscent of cell sorting in

embryonic development and is very different from the mechanisms that have been previously studied[20-24], which require differential cell adhesion or repulsion and postulate that cell sorting relaxes the tissue towards a free energy minimum, as in thermal systems.

2 Model

We consider a system of N monodisperse disks of radius R in a square box of length L. The overdamped dynamics is governed by Langevin equations for the position $\mathbf{r}_i$ of the center of the i-th disk and a unit vector $\mathbf{u}_i = (\cos\theta_i, \sin\theta_i)$ along the axis of self propulsion,

$$\partial_t \mathbf{r}_i = v_0 \mathbf{u}_i + \mu \sum_j \mathbf{F}_{ij}, \qquad \partial_t \theta_i = \eta_i(t), \qquad (1)$$

where v_0 is the active (self-propulsion) speed and μ the mobility. The particles interact via short-range repulsive forces $\mathbf{F}_{ij}$ proportional to the overlap between two disks, $\mathbf{F}_{ij} = k(2R - r_{ij})\hat{\mathbf{r}}_{ij}$, with $\mathbf{r}_{ij} = \mathbf{r}_i - \mathbf{r}_j = \hat{\mathbf{r}}_{ij} r_{ij}$, and k a force constant. The angular noise η is white, with $<\eta_i(t)\eta_j(t')> = 2D_r \delta_{ij} \delta(t - t')$ and D_r the rotational diffusion rate. Large immobile particles are glued to the walls of the box to implement the confinement and to suppress crystallization. At low density, each disk performs a persistent random walk and is diffusive at long times ($t \gg D_r^{-1}$), with an effective diffusion constant $D_a = v_0^2/2D_r$ [6]. We treat D_r as an independent parameter because in many realizations, including bacterial suspensions[25] and active colloids[26], the rotational noise is athermal. In these systems, D_a is also typically two orders of magnitude larger than the thermal diffusivity, and so we neglect thermal noise in Eq. (1).

Lengths and times are in units of the particle radius R and the elastic time $(\mu k)^{-1}$. Unless otherwise noted, the size of the box is $L = 83$. Particle positions are initialized with a uniform random distribution inside the box, and orientations are random over the interval $[0, 2\pi]$. Equations (1) are integrated numerically using an Runge-Kutta algorithm for $t = 9000$ timesteps. This time interval is sufficient to ensure that the density profile of the system has reached steady state. We explore the behavior of the system by varying the active velocity v_0, the rotational diffusion rate D_r, and the packing fraction $\phi = N\pi R^2/L^2$ [*].
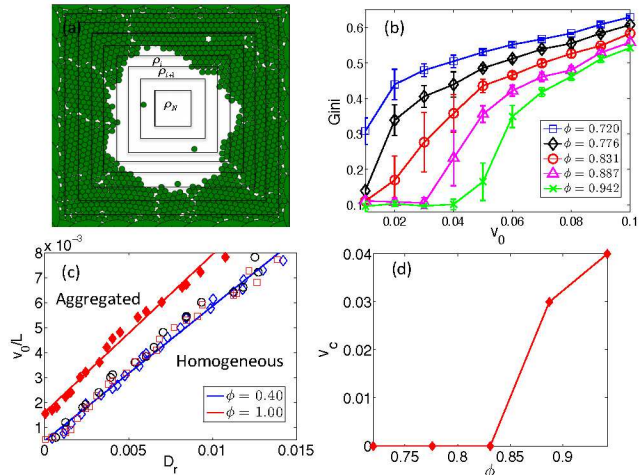

Fig. 2 (a) Diagram of nested square strips. (b) Gini coefficient vs. v_0 at various packing fractions. The rotational noise is $D_r = 5 \times 10^{-5}$ and the total simulation time is $T = 9000$. (c) Phase boundaries separating aggregated and homogeneous states in the plane of v_0/L vs D_r. The open symbols are for $\phi = 0.40$ and $L = 83, 110, 130$ (circles, squares, diamonds). The straight line is a fit to that data with $v_0 = ALD_r$, where $A = 0.5402$. Filled diamonds are for $\phi = 1.00$ and $L = 83$. The total simulation time is $T = 2000$. (d) Critical speed at $D_r \to 0$ vs. packing fraction.

3 Aggregation and segregation

3.1 Wall aggregation

To quantify wall aggregation and the resulting density inhomogeneities we divide the system in n_Δ nested square strips of thickness Δ (Fig. 2(a)) and calculate the gini coefficient[27], given by $g = \frac{1}{2N^2|\bar{\rho}|} \sum_i \sum_j |\rho_i - \rho_j|$, with $\bar{\rho}$ the mean density, ρ_i the number density of particles in the i-th strip, and $\Delta = 2R$. The gini coefficient provides direct information of the spatial organization of density inhomohgeneitites. It approaches 0 when the density is homogeneous Fig.1(b)(c) and 1 when all particles are at the wall Fig.1(a). The boundary separating homogenous states from aggregated states where the particles accumulate at the walls is obtained by a linear fit to isosurfaces of the gini coefficient, and corresponds to $g = 0.5$, above which we say the system is wall-aggregated as shown in Fig 2 (c) for different values of ϕ. At low ϕ, aggregation occurs when D_r is small and particles travel ballistically across the container. The phase boundary is well-described by $v_0/L \propto D_r$, which is the solid line through the open circles in Fig. 2 (c). The gini coefficient increases continuously with v_0/D_r, consistent with the result in[11]. At high ϕ, a finite

---

value $v_c(\phi)$ is required for wall aggregation even in the limit $D_r \to 0$, as shown by the solid line through the closed diamonds in Fig. 2 (c). The dependence on ϕ is seen in Fig. 2 (b), where the gini coefficient immediately rises from its minimal value for $\phi < 0.83$, and only rises at a finite v_c for $\phi > 0.88$. The critical v_c as a function of ϕ is shown in Fig. 2(d). The onset of a finite threshold for aggregation at $\phi \simeq 0.88$ coincides with the jamming point for monodisperse passive hard disks at zero temperature[17]. The result is also consistent with active jamming in a disordered landscape[28].

3.2   Pressure

To quantify force distribution in our active fluid, we have evaluated the pressure both in the homogeneous and wall-aggregated states. We define the pressure using the Irving-Kirkwood (IK) expression for the stress tensor given below [29], augmented by a contribution from self-propulsion. We have checked that this yields the same result as measuring the force per unit length on the walls of the container at all packing fractions. This demonstrates that the generalized IK formula proposed below is the correct expression for evaluating the mechanical pressure of an active system. The stress tensor $\sigma_{\alpha\beta}$ (with $\alpha, \beta = x, y$) is naturally separated in a contribution from interactions and an active contribution, as $\sigma_{\alpha\beta} = \sigma_{\alpha\beta}^{int} + \sigma_{\alpha\beta}^{a}$, with

$$\sigma_{\alpha\beta}^{int} = \frac{1}{L^2}\left\langle \sum_{i \neq j} F_{ij}^{\alpha} r_{ij}^{\beta} \right\rangle, \ \sigma_{\alpha\beta}^{a} = \frac{1}{L^2}\left\langle \sum_{i} F_{i,a}^{\alpha} r_i^{\beta} \right\rangle, \quad (2)$$

where $\mathbf{F}_{i,a} = (v_0/\mu)\mathbf{u}_i$ is the active force on each disk. The pressure is the trace of the stress tensor, $P = \sigma_{\alpha\alpha}/2 = P_{int} + P_a$, shown in Fig. 3(a) as a function of ϕ for a small rotational diffusion rate $D_r = 5 \times 10^{-5}$. For small D_r, where the system aggregates at the walls and exhibits strong density and pressure inhomogeneities (Fig. 1(a)), the pressure is a strongly non-monotonic function of density and starts decreasing at $\phi \simeq 0.672$, well below jamming. At this packing fraction the density gradients start to smoothen, and the pressure becomes more homogeneous, as shown in Fig. 4(a), which displays the interaction force between particles as a function of distance to the wall. Fig. 4(b) shows the gini coefficients of density and pressure, demonstrating that the pressure inhomogeneity is a direct consequence of density inhomogeneity. Meanwhile, particles are caged by their neighbors. This leads to "self-trapping", resulting in a suppression of their effective self-propulsion speed, as discussed in recent work on active phase separation[5–7,30–32]. In this region, although the system is fairly homogeneous, the transmission of force is impeded by crowding, resulting in an increased effective rotational diffusion rate and a sharp decrease in pressure. This description is supported by the correlation between the compressibility and homogeneity of the system, Fig 4(b). The decrease in the

forces that particles are able to transmit to the walls is most dramatic in the active pressure, that seems to essentially vanish near $\phi = 0.907$, the packing fraction corresponding to perfect crystalline order in a triangular lattice. Fig. 3(b) shows that the pressure non-monotonicity diminishes with increasing D_r, and the active system exhibits thermal-like behavior when $v_0/L \ll D_r$, as suggested by the curve of filled circles. The analogy with a thermal system and the notion of effective temperature can, however, be made precise only in the low density limit. At finite density, repulsive interactions affect the active system quite differently from its thermal counterpart even in the limit of large D_r, and the pressure of the thermal system increases much faster than the active one, as shown in Appendix D. In all cases, the pressure increases steeply above $\phi \simeq 0.88$ due to enforced overlap.
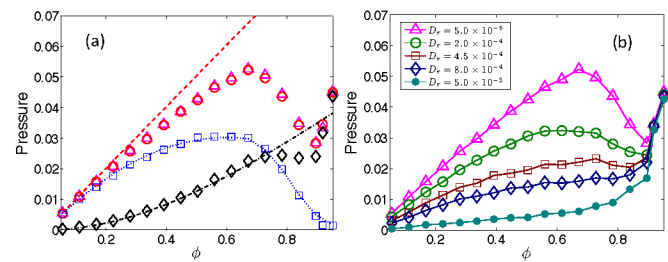

Fig. 3 (a) Total pressure calculated from the IK formula (triangles) and as the force on the walls (circles) as a function of packing fraction at $v_0 = 0.02$ and $D_r = 5 \times 10^{-5}$. The two calculations yield the same result. Also shown are the interaction (black diamond) and active (blue squares) contributions to the pressure. The dashed magenta line is the calculated ideal gas pressure with no fitting parameters. The black dot-dashed line is the calculated interaction pressure with $c = 1.2$. The blue dotted line is the calculated active pressure with a density-dependent active velocity $v(\phi)$ and effective rotational diffusion rate $D_r^{eff}(\phi)$. (b) Total pressure for various rotational noise D_r.

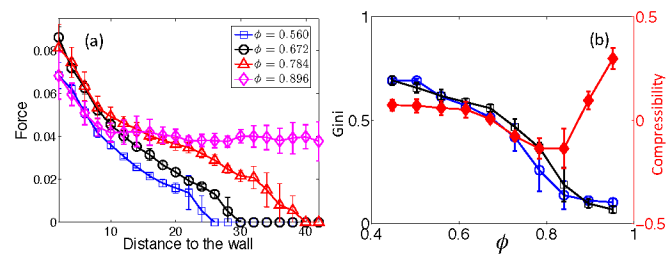**Fig. 4** (a) Interaction force as a function of distance to the wall for various packing fractions ϕ. (b) Gini coefficient of density (circles), gini coefficient of force (squares) and compressibility (filled diamonds) vs. packing fractions at $v_0 = 0.02$, $D_r = 5 \times 10^{-5}$.

The active pressure can be calculated analytically at low density from the Langevin equations (1) neglecting interac-

tions. The result corresponds to the pressure of an active ideal gas, also discussed in[33,34]. Using $\langle u_{i\alpha}(t)u_{j\beta}(t')\rangle = e^{-D_r|t-t'|}\delta_{ij}\delta_{\alpha\beta}$, we find $P_0(t) = \frac{\rho v_0^2}{2\mu D_r}\left(1 - e^{-D_r t}\right)$ for the ideal active gas pressure. In a container of side L, active particles eventually get stuck at the wall. For small, but finite D_r, we then define the ideal gas active pressure as $P_0 = P_0(t = L/v_0)$, where L/v_0 is the time required by an active particle to travel ballistically through the container. The resulting expression

$$P_0 = \frac{\rho v_0^2}{2\mu D_r}\left(1 - e^{-D_r L/v_0}\right) \tag{3}$$

interpolates between the thermal limit $P_0 \approx \rho v_0^2/(s\mu D_r)$ for $D_r \gg v_0/L$ and the value $P_0 \approx \rho v_0 L/(2\mu)$ for $D_r \ll v_0/L$ corresponding to N disks each exerting a uniform force v_0/μ on the walls. The ideal pressure of an active gas is shown in Fig. 3(a) as a dashed line and fits the data at low density. At moderate density the pressure remains a monotonically increasing function of density, but is suppressed relative to the ideal gas expression. This deviation can be understood as arising from "self-trapping", which yields a density-dependent effective active velocity[6] $v(\phi) = v_0(1 - \lambda\phi)$. At high density, however, the active pressure shows a nonmonotonic behavior and decreases with increasing density. This nonmonotonicity is indicative of strong caging and cannot be described solely in terms of a suppression of active speed. A mean-field formula that fits the pressure over the entire range of density can be obtained by assuming that caged active particles repeatedly change direction of motion due to interaction, resulting in an enhanced effective rotational diffusion rate, $D_r^{eff}(\phi) = \Theta(\phi - \phi_c)\exp[\alpha(\phi - \phi_c)]$, which characterizes the rate of change in the direction of the actual velocity $\mathbf{v}_i = \partial_t\mathbf{r}_i$, with $\Theta(\phi - \phi_c)$ the Heaviside step function, and ϕ_c the critical packing fraction above which this caging effect kicks in. We emphasize that this occurs well below jamming and ϕ_c generally depends on the active speed v_0, as discussed in Appendix B. A fit to this mean-field theory that incorporates density-dependent velocity and rotational diffusion rate is shown in Fig. 3(a) as a dotted line.

On the other hand, a simple expression for the interaction pressure can be obtained by modeling the system as concentric layers of particles aggregated at the walls and assuming that the particle overlap, hence the force that each layer exerts on the walls, increases linearly as the wall is approached. This estimate, described in Appendix A, gives $P_{int} = c\left(\frac{Lv_0}{16R}\phi^2 - \frac{Lv_0}{48R}\phi^3\right)$, with c a fitting parameter. A fit to this expression with $c = 1.2$ is shown in Fig. 3.

3.3 Active mixtures and segregation

The mechanisms responsible for athermal phase separation[6] and wall aggregation of purely repulsive self-propelled par-

ticles have remarkable consequences in mixtures. We simulate a binary mixture of small (S) and large (L) self propelled particles with diameter ratio 1.4 to prevent crystallization. Although different in size, they interact via the same harmonic soft repulsive potential, with *equal* force constants $k_{SL} = k_{SS} = k_{LL}$, and with dynamics described by Eqs. (1). The self-propulsion speeds are v_S and v_L respectively, and to reduce the number of parameters we have assumed equal mobilities for both types of particles. To quantify the spatial dis-
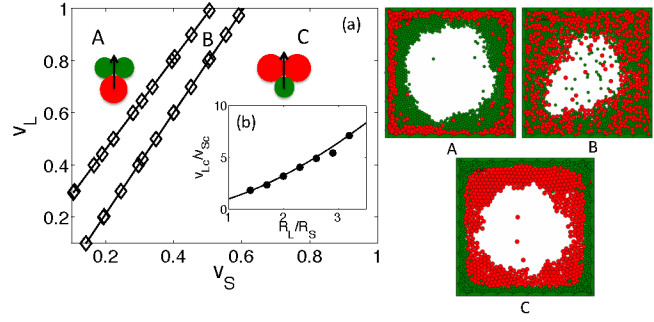

Fig. 5 (a) Phase diagram showing the segregated and homogeneous states as functions of the active velocities v_S and v_L (small particles are green and large ones are red) for $D_r = 5 \times 10^{-5}$ and a total packing fraction $\phi = 0.9$, with each species occupying half of the packing fraction. (b) Analytical calculation identifying when particles with a given active velocity and radius ratio are able to overcome mean-field elastic energy barriers (solid line). Onset of particle segregation in simulations (data points). The remarkable agreement with no fit parameters demonstrates that segregation is driven by asymmetric elastic energy barriers. A-C are snapshots of segregated and homogeneous states. The labels A, B, C correspond to the states marked in the phase diagram. (†Supplementary Movies 4-5)

tribution of the two particle types, we define a segregation coefficient S:

$$S = \frac{\sum_i |\rho_i^L - \rho_i^S|}{\sum_i \max[\rho_i^L, \rho_i^S]} \tag{4}$$

where the shell width Δ is the large particle diameter and $\rho_i^{S,L}$ is the density of small/large particles in the i-th shell. With this definition, $S \to 0$ for a uniform distribution of L and S disks, and $S \to 1$ for complete segregation.

When these purely repulsive disks are exactly the same except for their size ($v_S = v_L$), the system spontaneously segregates so that the small particles aggregate near the walls and the large particles are closer to the center of the box. We choose a critical value of $S = 0.5$ to differentiate segregated state from mixed state.

To better understand this suprising result, we study a phase diagram of the segregation as a function of the two self-propulsion speeds v_S and v_L, shown in Fig. 5. We find three

5   APPENDIX A: INTERACTION PRESSURE OF THE AGGREGATED STATE

distinct states: (A) a segregated state where all the large (red) disks have accumulated at the wall, with the small (green) ones closer to the center, (B) a mixed state where the particles have accumulated at the wall, but they are homogeneously distributed, hence $S \sim 0$ and (C) a segregated state where the small disks are near the walls and the large ones are near the center. The lower left hand corner of Fig 5 demonstrates that if both the small and large particle velocities are too small, the system remains mixed. This suggests that particles must overcome a finite energy barrier in order to segregate. To quantify and test this assumption, we let v_{Sc} (v_{Lc}) denote the critical velocity of the small (large) particles in the limit $v_L \rightarrow 0$ ($v_S \rightarrow 0$). To estimate v_{Sc}, we derive an analytic expression for the velocity required for an active small particle to cross through two immobile large particles in contact with zero overlap, assuming that the small particle is moving directly perpendicular to the pair, as illustrated in Fig. 5 (See Appendix C for details). This is a mean-field theory for energy barriers in a system exactly at the jamming transition. We derive a similar expression for v_{Lc}, and calculate the ratio v_{Lc}/v_{Sc}. While the data in Fig. 5(a) are for a bidisperse mixture with diameter ratio 1.4, we calculate the velocity ratio as a function of the diameter ratio $x = R_L/R_S$, obtaining

$$\frac{v_{Lc}}{v_{Sc}} = x^{-\frac{2}{3}} \frac{[1-(1+x)^{-2/3}]^{\frac{1}{2}}[(1+x)^{2/3}-1]}{[1-(1+\frac{1}{x})^{-2/3}]^{\frac{1}{2}}[(1+\frac{1}{x})^{2/3}-1]} \qquad (5)$$

This function $\frac{v_L}{v_S}(x)$ is plotted in Fig 5(b) as a solid line. We then extract numerical values of v_{Lc}/v_{Sc} from the segregation boundary in simulations with different values of R_L/R_S. These numerical results are the data points in Fig 5 (b). The remarkable overlap between the theory and simulation suggests that our mean field theory is valid and that asymmetric energy barriers for particles moving across one another are responsible for segregation.

We emphasize that the phenomenon of active segregation is intrinsically different from the "Brazil Nut Effect"[35], where a bidisperse granular mixture segregates under external shaking. Our soft active particles are individually driven rather than agitated through boundary forces. As a result, size segregation in our active system is driven by the asymmetry of the energy barriers imposed by soft repulsive interaction between particles as supported by the outstanding agreement between analytical and numerical results shown in Fig 5(b), rather than by the "void-filling"[35] or "granular convection"[36] mechanisms proposed to explain the "Brazil Nut Effect".

4   Conclusions

We have demonstrated that in the limit of small rotational noise, spherical self-propelled particles spontaneously accumulate at the walls of a container in the absence of any align-

ment or attractive interactions. At high density there is a finite threshold speed $v_c(\phi)$ for wall aggregation in the limit $D_r \rightarrow 0$. This speed vanishes at low density and becomes finite near the jamming transition, suggesting that the particles must overcome a finite yield stress to rearrange and accumulate at the walls. The pressure displays a startling non-monotonic dependence on density. When particles are aggregated at the walls the pressure increases with density, as the particles pack densely to optimize force transmission. Eventually, as the system approaches the jamming transition, both density and force distribution become more homogeneous and the particles become caged by their neighbors, losing the ability to self-organize to optimally transmit stress. The net result is that the pressure decreases drastically with increasing density. We are currently implementing simulations at constant pressure to interpret this surprising effect that could never happen in a thermal system.

In a mixture of active disks of two sizes we observe segregation in the absence of any adhesive interaction, which may be relevant to cell sorting[14–16] and cell-assisted size segregation of colloidal particles[37].

5   Appendix A: Interaction pressure of the aggregated state

For simplicity, we consider a completely aggregated state, where the active force is balanced by the interaction force. We work in a coordinate system with axes along the principal direction of the stress tensor, and therefore drop the label of component for force and particle position. The trace of the stress is then given by

$$\sigma_{\alpha\alpha} = \frac{1}{L^2} \sum_{i \neq j} F_{ij} r_{ij} , \qquad (6)$$

where the summation is over all interacting pairs. As illustrated in Fig 6, the interaction forces are transmitted through chains of particles, resulting in a larger interaction force/stress closer to the wall. Given that our repulsive force is a linear function of overlap, we assume that the stress increases linearly as the wall is approached. This assumption is supported by Fig 4(a) in the paper. To proceed, we divide the system into N nested particle layers, as shown in Fig 6. Each layer has the width of a particle diameter $2R$, area A_n and occupies a fraction $\phi_n = A_n/L^2$ of the entire system's area. We assume that ϕ_n is also the packing fraction of particles in the n-th layer. Approximating the area of a layer as the sum of the area of four equal strips, we can write

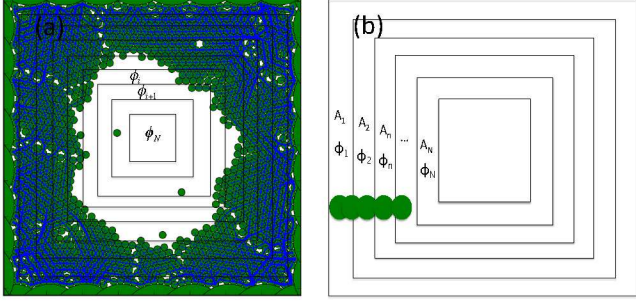$$A_n = 8LR - 32R^2(n-1) . \qquad (7)$$

Fig. 6 (a) Snapshot of an aggregated state with force chains (blue). The nested particle layers are also displayed. The overlap between particles increases as they approach the wall, indicating an inhomogeneous distribution of pressure, which is maximum at the wall, as shown by the force chains. (b) The aggregated state is modeled as a collection of N nested layers of particles, with a linear increase of overlap (or pressure) as the wall is approached. Each layer has area A_n and is occupied by active particles of packing fraction ϕ_n.

We assume that the total packing fraction ϕ of the system is equal to the sum of ϕ_n,

$$\phi = \sum_{n=1}^{N} \phi_n = \frac{1}{L^2}\left(8LRN + 16NR^2 - 16R^2N^2\right) . \tag{8}$$

Solving Eq. (8) for N in terms of ϕ, we obtain

$$N \simeq \frac{L}{8R}\phi + \mathcal{O}(R/L) . \tag{9}$$

Now we proceed to calculate the stress. When the system is completely aggregated, the interaction forces are balanced by the active forces $F_a = v_0/\mu$. Assuming that the force increases linearly as we approach the wall, and imposing force balance between the interaction force F_{ij}^n on particle i in the n-th layer due to particle j in the $n-1$ layer and the active forces, we can write

$$F_{ij}^n = (n-1)F_a = (n-1)\frac{v_0}{\mu} . \tag{10}$$

The stress in the nth layer is then given by

$$\sigma_{\alpha\alpha}^n = \frac{1}{A_n}\sum_{i \neq j} F_{ij}^n r_{ij}^n . \tag{11}$$

Inserting Eq. (10), we obtain

$$\sigma_{\alpha\alpha}^n = \frac{1}{A_n}\sum_{1}^{CN_n/2}(n-1)\frac{v_0}{\mu}[2R - (n-1)\frac{v_0}{k\mu}] , \tag{12}$$

where C is a fitting parameter corresponding to the average contact number of a particle and N_n is the number of particles

in the nth layer. Expanding Eq. (12) and keeping only terms to lowest order in v_0, we obtain

$$\sigma_{\alpha\alpha}^n = c\phi_n(n-1)v_0 , \tag{13}$$

where $c = \frac{C}{\pi R\mu}$ is a rescaled fitting parameter. Using $\phi_n = \frac{A_n}{L^2}$ and summing over the layers, we obtain an expression for the total stress as

$$\sigma_{\alpha\alpha} = \sum_{n=1}^{N}\sigma_{\alpha\alpha}^n \simeq \int_1^N \sigma_{\alpha\alpha}^n(n)dn$$
$$= \int_1^N\left[\frac{8Rcv_0}{L}(n-1) - \frac{32R^2cv_0}{L^2}(n-1)^2\right]dn \tag{14}$$

where the sum over layers has been replaced by an integration. Carrying out the integration we find

$$\sigma_{\alpha\alpha} = \frac{4Rcv_0}{L}(N-1)^2 - \frac{32R^2cv_0}{3L^2}(N-1)^3$$
$$\simeq \frac{4Rcv_0}{L}N^2 - \frac{32R^2cv_0}{3L^2}N^3 = c\left(\frac{Lv_0}{16R}\phi^2 - \frac{Lv_0}{48R}\phi^3\right) \tag{15}$$

The pressure of the system is defined as

$$P = \frac{\sigma_{\alpha\alpha}}{2} \tag{16}$$

To fit the data for $k = 1$, $\mu = 1$, $R = 1$ and $L = 80$ yields $c = 1.2$, corresponding to an average contact number of 6.

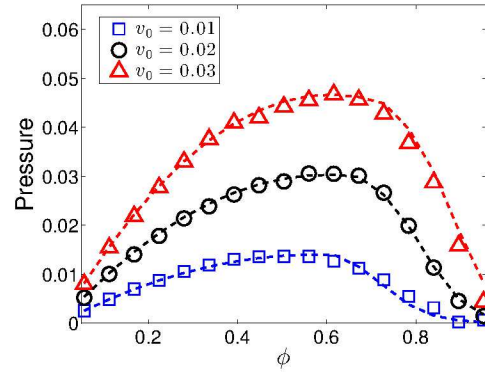# 6   Appendix B: Non-monotonic active pressure

Fig. 7 Markers: Active pressure as a function of packing fraction for various active speeds v_0 and $D_r = 5 \times 10^{-5}$. Dashed line: Fitting using expression of ideal active gas pressure with density-dependent velocity and density-dependent effective rotational diffusion rate.

The suppression of self-propulsion due to caging can be incorporated in a mean-field fashion by replacing the active

speed v_0 in the ideal gas pressure by a density-dependent speed $v(\phi)$, as suggested by recent work on phase separation of active particles[6]. We also speculate that crowding effectively increases the rate of rotational diffusion as particles rattle around the confining cage and incorporate this effect into a density-dependent effective rotational diffusion rate $D_r^{eff}(\phi)$, which is enhanced at packing fraction above ϕ_c, where the active pressure starts to decrease sharply. A fit to the active pressure for various active speeds v_0 using the ideal gas formula $P_0 = \frac{\rho v_0^2}{2\mu D_r}\left(1 - e^{-D_r L/v_0}\right)$ with $v(\phi) = v_0(1 - \lambda\phi)$ replacing v_0 and $D_r^{eff}(\phi) = \Theta(\phi - \phi_c)\exp[\alpha(\phi - \phi_c)]$ replacing D_r, where $\Theta(\phi - \phi_c)$ is the Heaviside step function, is shown in Fig. 7 as dashed lines. The fitting parameters are $\lambda = 0.8$ and $\alpha = 13$. The critical packing fraction ϕ_c increases with active speed v_0, where $\phi_c = 0.616, 0.672, 0.728$ corresponds to $v_0 = 0.01, 0.02, 0.03$ respectively. This suggests that activity counteracts the effect of crowding, which is consistent with the "unjamming" of the system as activity increases (Fig. 2(b)).

7   Appendix C: Segregation barriers

To evaluate the barrier that particles must overcome for segregation, we consider the geometry shown in Fig. 8 displaying a small active particle of radius R_S that has to make its way through two immobile large particles of radius R_L. For the small particle to travel through the barrier imposed by the two large ones, the active force v_0/μ has to overcome the maximum of the repulsive force F_{rep}. This defines a critical active velocity v_{Sc} for the small particle. To calculate this barrier we
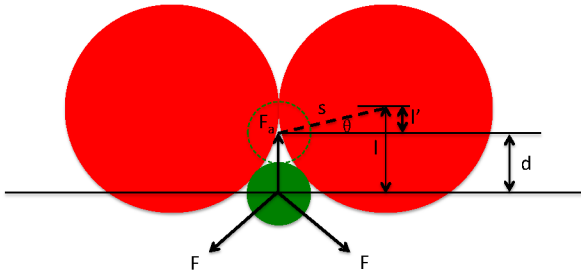

Fig. 8 Minimal model used to evaluate the barriers of segregation: a small active particle pushing its way through two adjacent, immobile large particles. R_S and R_L are the particles' radii. The small particle initially just touches its neighbors, then travels a distance d vertically with active velocity $F_a = v_0/\mu$. F is the repulsive force between two particles. Other geometrical quantities are as labelled.

assume that the small active particle initially just touches its neighbors, then travels upward a distance of d. At this point, the net repulsive force is

$$F_{rep} = 2F\sin\theta \,, \tag{17}$$

where $F = k[(R_L + R_S) - \sqrt{(l-d)^2 + R_L^2}]$ is the repulsive force between two particles and $\sin\theta = l'/s$. Geometrical considerations lead to $l' = l - d$, $s = \sqrt{(l-d)^2 + R_L^2}$ and $l = \sqrt{r^2 + 2R_S R_L}$, allowing us to express F_{rep} solely in terms of d.

The critical active velocity v_{Sc} is defined as the maximum value of $\mu F_{rep}(d)$. This gives

$$v_{Sc} = 2\mu k[(R_L + R_S)R_L^2]^{1/3}[1 - (1 + \frac{R_S}{R_L})^{-2/3}]^{1/2}$$
$$\times [(1 + \frac{R_S}{R_L})^{2/3} - 1] \,. \tag{18}$$

This is the critical velocity of an active particle with radius R_S pushing through two immobile particles of radius R_L. The critical velocity for the reversed configuration, corresponding to a particle of radius R_L pushing through two particles of radius R_S, can be obtained by interchanging R_S and R_L. Segregation occurs when either species has an active velocity above the critical value. Note that particles with different radii have different critical velocities. If, for instance, $R_S < R_L$, then $v_{Sc} < v_{Lc}$, and small particles will aggregate to the outside, next to the wall, when both species have the same active velocity.

Finally, the ratio of active velocities of the two species can be written as a function of their radii ratio as

$$\frac{v_{Lc}}{v_{Sc}} = x^{-\frac{2}{3}}\frac{[1 - (1+x)^{-2/3}]^{\frac{1}{2}}[(1+x)^{2/3} - 1]}{[1 - (1+\frac{1}{x})^{-2/3}]^{\frac{1}{2}}[(1+\frac{1}{x})^{2/3} - 1]} \,, \tag{19}$$

where $x = R_L/R_S$. This result is compared with the numerical result in Fig.5(b) of the paper. The excellent agreement supports our simple model.

8   Appendix D: Comparison with thermal gas

In the limit $v_0/L \ll D_r$ the pressure of an ideal active gas given in Eq. (3) takes the form of the pressure of an ideal thermal gas, with an effective temperature $k_B T_{\text{eff}} = v_0^2/(2\mu D_r)$, corresponding to a thermal diffusivity $D_t = \mu k_B T_{eff} = \frac{v_0^2}{2D_r}$. This suggests that in this limit it may be possible to map the active system onto a thermal one with an effective temperature. Figure 9 compares the pressure of an active gas for $v_0 = 0.02$ and $D_r = 0.005$ to that of a thermal gas with the corresponding value $D_t = 0.04$. Also shown is the analytical expression of Eq. (3). Although the three curves overlap at very low density, the pressure of the thermal gas rises much more rapidly than that of the active gas with increasing packing fraction, indicating that repulsive interactions are more effective in building up pressure in the thermal system. Surprisingly, the pressure in the active system falls slightly below the active ideal gas limit at intermediate packing fractions.
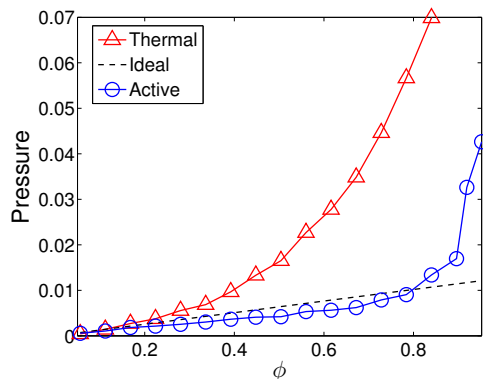
Fig. 9 Pressure as a function of packing fraction for an active system with $v_0 = 0.02$, $D_r = 0.005$ and $L = 80$ (blue circles) and of a thermal system with $D_t = 0.04$ (red triangles). The black dashed line is the calculated expression for pressure for the ideal active gas pressure given in Eq. (3).

Acknowledgements

References

1 M. C. Marchetti, J. F. Joanny, S. Ramaswamy, T. B. Liverpool, J. Prost, M. Rao and R. A. Simha, *Rev. Mod. Phys.*, 2013, **85**, 1143–1189.

2 T. Vicsek, A. Czirók, E. Ben-Jacob, I. Cohen and O. Shochet, *Phys. Rev. Lett.*, 1995, **75**, 1226–1229.

3 S. Ramaswamy, R. A. Simha and J. Toner, *Europhys. Lett.*, 2003, **62**, 196–202.

4 V. Narayan, S. Ramaswamy and N. Menon, *Science*, 2007, **317**, 105–108.

5 J. Tailleur and M. E. Cates, *Phys. Rev. Lett.*, 2008, **100**, 218103.

6 Y. Fily and M. C. Marchetti, *Phys. Rev. Lett.*, 2012, **108**, 235702 [5pages].

7 G. S. Redner, M. F. Hagan and A. Baskaran, *Phys. Rev. Lett.*, 2013, **110**, 055701.

8 E. Lauga, W. R. DiLuzio, G. M. Whiteside and H. A. Stone, *Biophys. J.*, 2006, **90**, 400–412.

9 A. P. Berke, L. Turner, H. C. Berg and E. Lauga, *Phys. Rev. Lett.*, 2008, **101**, 038102.

10 J. Tailleur and M. E. Cates, *Europhys. Lett.*, 2009, **86**, 60002.

11 J. Elgeti and G. Gompper, *Europhys. Lett.*, 2013, **101**, 48003.

12 A. Kudrolli, G. Lumay, D. Volfson and L. S. Tsimring, *Phys. Rev. Lett.*, 2008, **100**, 058001.

13 J. Elgeti and G. Gompper, *Europhys. Lett.*, 2009, **85**, 38002 (6pp).

14 E. Méhes, E. Mones, V. Németh and T. Vicsek, *PLoS one*, 2012, **7(2)**, p.e31711.

15 J. M. Belmonte, G. L. Thomas, L. G. Brunnet, R. M. C. de Almeida and H. Chaté, *Phys. Rev. Lett.*, 2008, **100**, 248702.

16 S. R. McCandlish, A. Baskaran and M. F. Hagan, *Soft Matter*, 2012, **8**, 2527–2534.

17 A. Donev, S. Torquato, F. H. Stillinger and R. Connelly, *Journal of Applied Physics*, 2004, **95**, 989.

18 S. A. Mallory, A. Šarić, C. Valeriani and A. Cacciuto, *Phys. Rev. E*, 2014, **89**, 052303.

19 D.Ray, C.Reichhardt and C. Reichhardt, *arXiv:1402.6372*, 2014.

20 M. Steinberg, *Science*, 1963, **141(3579)**, 401–8.

21 A. K. Harris, *J Theor Biol*, 1976, **61(2)**, 267–285.

22 R. Foty and M. Steinberg, *Dev Biol*, 2005, **278(1)**, 255–63.

23 M. Krieg, Y. Arboleda-Estudillo, P.-H. Puech, J. Käfer, F. Graner, D. J. Müller and C.-P. Heisenberg, *Nature Cell Biol.*, 2008, **10**, 429–436.

24 M. L. Manning, R. A. Foty, M. S. Steinberg and E.-M. Schoetz, *PNAS*, 2010, **107**, 12517–12522.

25 H. C. Berg, *E. coli in Motion*, Springer, New York, 2004.

26 J. Palacci, S. Sacanna, A. P. Steinberg, D. J. Pine and P. M. Chaikin, *Science*, 2013, **339**, 936–940.

27 L. Ceriani and P. Verme, *The origins of the Gini index: extracts from Variabilità e Mutabilità (1912) by Corrado Gini*, Springer US, 2012, vol. 10.

28 C. Reichhardt and C. O. Reichhardt, *arXiv:1402.3260*, 2014.

29 J. H. Irving and J. G. Kirkwood, *J. Chem. Phys.*, 1949, **18**, 6.

30 Y. Fily, S. Henkes and M. C. Marchetti, *Soft Matter*, 2014, **10**, 2132–2140.

31 M. E. Cates, *Rep. Prog. Phys.*, 2012, **75**, 042601 (14pp).

32 X. Yang, D. Marenduzzo and M. C. Marchetti, *Phys. Rev. E*, 2014, **89**, 012711.

33 B. M. Mognetti, A. Šarić, S. Angioletti-Uberti, A. Cacciuto, C. Valeriani and D. Frenkel, *Phys. Rev. Lett.*, 2013, **111**, 245702.

34 Y. Fily, A. Baskaran and M. F. Hagan, *arXiv:1402.5583*, 2014.

35 A. Rosato, K. J. Strandburg, F. Prinz and R. H. Swendsen, *Phys. Rev. Lett.*, 1987, **58**, 1038–1040.

36 J. B. Knight, H. M. Jaeger and S. R. Nagel, *Phys. Rev. Lett.*, 1993, **70**, 3728–3731.

37 V. K. Kodali, W. Roos, J. P. Spatz and J. E. Curtis, *Soft Matter*, 2007, **3**, 337–348.